Pathology-aware Virtual H&E Staining of Section-free Thick Tissues with Semantic Contrastive Guidance

Jintaek Oh*, Lulin Shi*, and Terence T. W. Wong

Translational and Advanced Bioimaging Laboratory, Department of Chemical and Biological Engineering, The Hong Kong University of Science and Technology, Hong Kong
ttwwong@ust.hk

Abstract. The conventional histopathology paradigm, while remaining the gold standard for clinical diagnosis, is inherently constrained by its lengthy processing time. The emergence of virtual staining in computational histopathology has catalyzed significant research efforts toward developing rapid and chemical-free staining techniques. However, current methodologies are primarily applicable to well-prepared thin tissue sections and lack the capability to effectively process the section-free thick tissues. In this work, we present a novel approach that utilizes fluorescence light-sheet microscopy to directly image thick tissue samples, followed by image translation to generate virtually stained hematoxylin and eosin (H&E) images. To overcome the insufficient exploration of pathological features in current methods, we introduce Semantic Contrastive Guidance (SemCG), which enforces morphological consistency between fluorescence inputs and H&E outputs. Additionally, we incorporate subtype-aware classification to enhance the discriminator's ability to learn domain-specific pathological knowledge. Experimental results demonstrate that our proposed modules offer an advantage in generating high-quality images. We anticipate that this sectioning-free virtual staining framework will have significant potential for clinical rapid pathology applications, offering a transformative improvement to current histological workflows. Our code is available at https://github.com/commashy/SemCG-Stain.

Keywords: Virtual staining · Computational pathology · Section-free microscopy · Generative adversarial network.

1 Introduction

Routine histological staining, a cornerstone technique in pathological diagnosis, predominantly relies on chemical reagents and sectioning processes [4,16]. This conventional methodology typically requires an extensive preparation period spanning several days, encompassing multiple critical steps: tissue fixation, dehydration, paraffin embedding, sectioning, dewaxing, and staining. The

* contributed equally

prolonged processing time, coupled with the necessity for specialized laboratory infrastructure and skilled personnel, significantly restricts its applicability in rapid histopathology scenarios. These limitations become particularly pronounced in time-critical clinical situations, such as intraoperative tissue examination where surgeons require immediate pathological feedback to guide surgical decisions [20,12]. These constraints have driven the scientific community to explore alternative approaches that can provide comparable histological information while overcoming the temporal and technical limitations of conventional methods.

Virtual histological staining has emerged as a promising direction in medical image computing, allowing the rapid conversion of non-H&E tissue scans to conventional H&E-like images [19,18,26,9,3,10]. This paradigm can significantly reduce workload and accelerate pathological assessments in both research and clinical settings. However, the majority of the aforementioned research has predominantly focused on well-prepared thin sections ($\sim$3 to 5 μm in thickness). The acquisition and preparation of these thin sections—including paraffin embedding, tissue sectioning, and chemical dewaxing—not only lead to prolonged turnaround times but also impose significant demands on laboratory infrastructure. Recent advancements in section-free imaging techniques have revolutionized the visualization of unprocessed thick tissue samples, bypassing the need for traditional sectioning procedures [5,6]. Several pioneering studies have explored virtual H&E staining approaches using section-free microscopy techniques [8,13,1]. However, these methods predominantly rely on point-scanning microscopy systems for large-scale tissue imaging, such as photoacoustic microscopy and confocal microscopy, which inherently suffer from low acquisition speed due to their sequential scanning nature. In an effort to overcome this limitation, recent advancements have demonstrated the potential of wide-field microscopy systems combined with cycleGAN architectures for rapid H&E staining generation [2,25,24]. While these approaches have shown promise in accelerating the virtual staining process, they are fundamentally constrained by their reliance on the basic cycleGAN framework, which lacks sophisticated mechanisms for precise control over complex pathological features and tissue patterns. This limitation becomes particularly evident when dealing with heterogeneous human tissue with cancer which is crucial for accurate pathological diagnosis.

In this work, we introduce SemCG-Stain, an innovative virtual staining framework achieving H&E-equivalent image generations from thick tissue scans, facilitating rapid, sectioning-free, and staining-free tissue analysis. Our key contributions can be summarized as follows:

1. Semantic Contrastive Guidance (SemCG): We propose a contrastive loss leveraging embeddings from a pathology-specific large vision model, PLIP [7], encouraging consistent morphological features between fluorescence inputs and target H&E outputs.
2. Pathology-aware Discriminator (PathD): A multi-scale adversarial module incorporating subtype-aware classification signals is employed to effectively integrate domain-specific pathological knowledge.

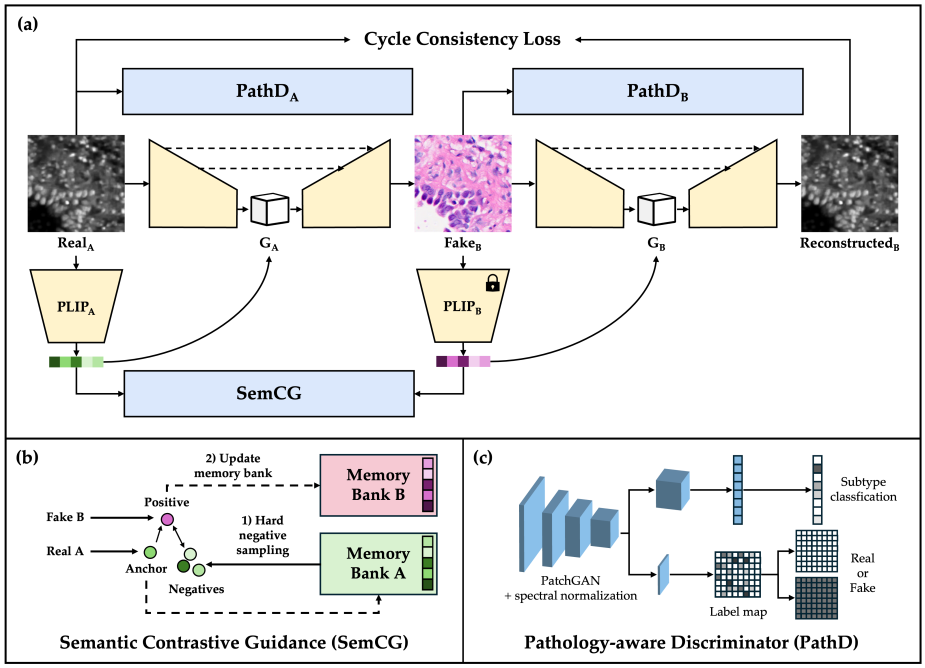

Fig. 1. Structure of the proposed SemCG-Stain. (a) The overall SemCG-Stain illustration. (b) The training process of SemCG. (c) The structure of the PathD.

3. Experiments conducted on sectioning-free human lung tissue samples demonstrate that our proposed model surpasses other baseline models commonly employed in the virtual staining domain, achieving superior performance in both image quality and clinical pathological relevance.

2 Methodology

SemCG-Stain translates the fluorescence image of thick tissue into H&E staining while preserving key pathological features. Firstly, we introduce SemCG to align high-level semantic features across modalities, and then we present the PathD for pathological knowledge fusion.

2.1 PLIP-Based Semantic Contrastive Guidance

To capture domain-invariant pathological features necessary for accurate image translation, we leverage semantic embeddings from the PLIP [7]. Although we adopt PLIP in this work, the framework is encoder-agnostic; any pathology-oriented CLIP variant such as CONCH [11] can be substituted without altering the rest of the pipeline. Our approach incorporates two specialized PLIP

encoders: $PLIP_A$ (partially fine-tuned), which is tailored for fluorescence images, and $PLIP_B$, which is dedicated to the target H&E domain. Specifically, for $PLIP_A$, we fine-tune the final two layers while keeping the remaining architecture frozen. This approach not only enables the model to adapt general pathology-relevant knowledge to the fluorescence domain but also ensures computational efficiency by minimizing the number of trainable parameters. In contrast, $PLIP_B$ remains entirely frozen to preserve its pretrained capability of embedding H&E images without additional modification. This dual-encoder strategy ensures robust feature extraction across domains while maintaining the integrity of domain-specific pathological representations.

For each mini-batch, patch-level embeddings are extracted from both fluorescence (via $PLIP_A$) and H&E (via $PLIP_B$) and stored in a continuously updated memory bank, the Memory bank **A** and **B** showing in Fig. 1. We then perform a *two-stage hard negative sampling*: (1) identify the top-k most similar embeddings (via cosine similarity) to the anchor embedding, and (2) randomly select a subset of these top-k to serve as "hard negatives." An InfoNCE [17]-based loss aligns corresponding fluorescence/H&E embeddings while repelling noncorresponding pairs. Formally, for an anchor embedding $\mathbf{e}_\mathrm{A}$ from a fluorescence image and a positive embedding $\mathbf{e}_\mathrm{b}$ from H&E, the basic contrastive loss is:

$$\mathcal{L}^{*}_{\text{contrast}} = -\log\left[\frac{\exp\left(\mathbf{e}_\mathrm{A}\cdot\mathbf{e}_\mathrm{B}\,/\,\tau\right)}{\exp\left(\mathbf{e}_\mathrm{A}\cdot\mathbf{e}_\mathrm{B}\,/\,\tau\right)\;+\;\sum_{n=1}^{N}\exp\left(\mathbf{e}_\mathrm{A}\cdot\mathbf{e}_n^{-}\,/\,\tau\right)}\right], \tag{1}$$

where τ is the temperature, $\{\mathbf{e}_n^-\}_{n=1}^N$ are the hard negatives sampled from the memory bank, and N is their number.

Furthermore, we compute the contrastive loss in both directions: $\mathcal{L}^{AB}_{\text{contrast}}$ for G_A and $\mathcal{L}^{BA}_{\text{contrast}}$ for G_B. The aggregated contrastive loss is then defined as:

$$\mathcal{L}_{\text{contrast}} = \lambda_{\text{clip\_contrast}}\left(\frac{\mathcal{L}^{AB}_{\text{contrast}} + \mathcal{L}^{BA}_{\text{contrast}}}{2}\right), \tag{2}$$

where $\lambda_{\text{clip\_contrast}}$ is a weighting factor, and this loss is subsequently incorporated into the overall generator objective.

2.2 Pathology-aware Discriminator and Stabilization Strategies

In this work, we focus on lung adenocarcinoma (LUAD), which includes several different subtypes within our dataset. Given the diverse pathological characteristics exhibited by different LUAD subtypes, we propose the PathD to guide the generator toward realism and subtype consistency. Building upon the multi-scale architecture introduced in [23], our PathD is designed to support subtype-aware discrimination by simultaneously generating a real/fake prediction map and predicting the subtype classification, as shown in Fig. 1c. The cross-entropy classification loss for the discriminator is given by:

$$\mathcal{L}_{\text{cls}} = -\,\mathbb{E}_{(\mathbf{x},c)\sim\mathcal{D}}\Big[\log P\big(c\,|\,D(\mathbf{x})\big)\Big], \tag{3}$$

To further stabilize adversarial training, we incorporate:

- **Spectral Normalization:** Applied to all convolutional layers to constrain the Lipschitz constant and mitigate abrupt gradient changes [15].
- **Zero-Centered Gradient Penalty:** Imposed on both real and generated samples to keep gradients near zero as the generator distribution approaches the real data distribution [14,21].

  and the zero-centered gradient penalty is:

$$\mathcal{L}_{\text{GP}} = \frac{\gamma}{2}\,\mathbb{E}_{x\sim p_{\text{real}}}\Big[\|\nabla_x D(x)\|_2^2\Big] + \frac{\gamma}{2}\,\mathbb{E}_{\hat{x}\sim p_{\text{fake}}}\Big[\|\nabla_{\hat{x}} D(\hat{x})\|_2^2\Big], \tag{4}$$

  where γ is a hyperparameter.

2.3 Loss Functions

In addition to the proposed contrastive loss $\mathcal{L}_{\text{contrast}}$, adversarial loss $\mathcal{L}_{\text{adv}}^{G}$ and classification loss $\mathcal{L}_{\text{cls}}$ described above, we retain the cycle-consistency principle from CycleGAN [27]. The total loss for the generator is formulated as:

$$\mathcal{L}_G = \mathcal{L}_{\text{adv}}^{G} + \lambda_{\text{cls}}\,\mathcal{L}_{\text{cls}} + \lambda_{\text{cycle}}\,\mathcal{L}_{\text{cycle}} + \lambda_{\text{contrast}}\,\mathcal{L}_{\text{contrast}}, \tag{5}$$

and the loss for the discriminator is:

$$\mathcal{L}_D = \mathcal{L}_{\text{adv}}^{D} + \lambda_{\text{cls}}\,\mathcal{L}_{\text{cls}} + \lambda_{\text{GP}}\,\mathcal{L}_{\text{GP}}, \tag{6}$$

where λ_{cls}, λ_{cycle}, $\lambda_{\text{contrast}}$, and λ_{GP} are weighting factors controlling the contribution of each term.

3 Experiments and Results

3.1 Datasets

We collected 12 lung tissue blocks spanning LUAD sub-types (Acinar, Micropapillary, Lepidic, Papillary, Solid, and Normal). Each specimen was formalin fixed at the hospital, transported to the laboratory, briefly surface-stained with DAPI (10 μg/mL, 1-2 min), and imaged intact with an open-top UV light-sheet microscope (266 nm excitation). The same blocks were subsequently processed through the standard histology workflow-fixation, paraffin embedding, microtome sectioning, and H&E staining-to yield corresponding thin-section reference slides. This produced a dataset of thick-tissue fluorescence images and thin-section H&E images. We allotted 8 samples to training and 4 to testing, maintaining subtype balance, and tiled both modalities into 256×256 patches, resulting in 29,835 training and 10,721 testing patches.

3.2 Implementation Details

Our model was implemented in `PyTorch` and trained on a single NVIDIA GeForce RTX 3090 GPU. We utilized the *Adam* optimizer with a learning rate of 2×10^{-5}, $\beta_1 = 0.0$, and $\beta_2 = 0.9$ for both the generator and discriminator. The learning rate remained constant until epoch 50, then decayed linearly to 0 by epoch 150. We set $\lambda_{cls} = 0.1, \lambda_{cycle} = 10, \lambda_{contrast} = 0.2$ and $\lambda_{GP} = 3$ in 5 and 6.

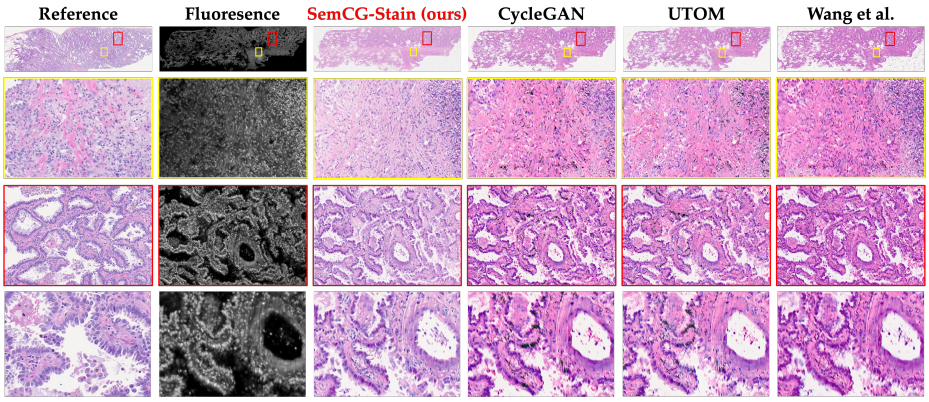

Fig. 2. Qualitative comparison of virtual H&E staining results. The top row shows the whole-slide view with red and yellow rectangles indicating regions of interest. The subsequent rows display zoomed-in views of these regions: the yellow region, rich in fibrotic components, and the red region, representing a papillary area.

3.3 Comparison with State-of-the-arts

To assess our framework's effectiveness, we compared it with state-of-the-art virtual staining methods, including CycleGAN [27], UTOM [9], and Wang et al. [22]. Fig. 2 qualitatively compares our method with baseline approaches. The top row shows a whole-slide view, revealing mismatched pathological features and missing information between the reference H&E and fluorescence images. This discrepancy arises because the reference H&E staining is performed on thin sections from the sample surface, while direct staining of the entire thick sample is impractical. Thus, the thin-section H&E staining only captures surface tissue structures, serving as a reference rather than an exact ground truth.

The subsequent rows provide zoomed-in views of the marked regions—yellow (fibrotic region) and red (papillary). While baseline models capture general features like background, foreground, and nuclear structures, they often generate over-saturated outputs with excessive pink and purplish tones. These exaggerated colors obscure subtle histopathological details and lead to inconsistent staining. In contrast, SemCG-Stain produces more natural and balanced stain tones, maintaining fine morphological details and enabling clearer differentiation of tissue structures, which is essential for accurate pathological analysis.

Table 1 summarizes quantitative results on the testing dataset using Fréchet Inception Distance (FID), Kernel Inception Distance (KID), and Inception Score (IS). Our method achieves an FID of 54.57, significantly lower than CycleGAN (76.51), UTOM (64.11), and Wang et al. (64.67), indicating closer alignment with real H&E image distributions. Additionally, our KID score of 2.47 outperforms the baselines (CycleGAN: 6.05, UTOM: 4.84, Wang et al.: 4.44), confirming superior feature-level similarity. Finally, our IS of 3.39 surpasses baseline scores, demonstrating enhanced realism and image quality.

	FID↓	KID (×100)↓	IS↑
CycleGAN [27]	76.51	6.05±0.34	3.02±0.07
UTOM [9]	<u>64.11</u>	4.84±0.24	3.05±0.04
Wang et al. [22]	64.67	<u>4.44±0.21</u>	<u>3.28±0.06</u>
SemCG-Stain (ours)	**54.57**	**2.47±0.13**	**3.39±0.06**

*__Bold__ and <u>underlined</u> indicate the best and the second-best results, respectively.
Table 1. Quantitative evaluation on testing data.

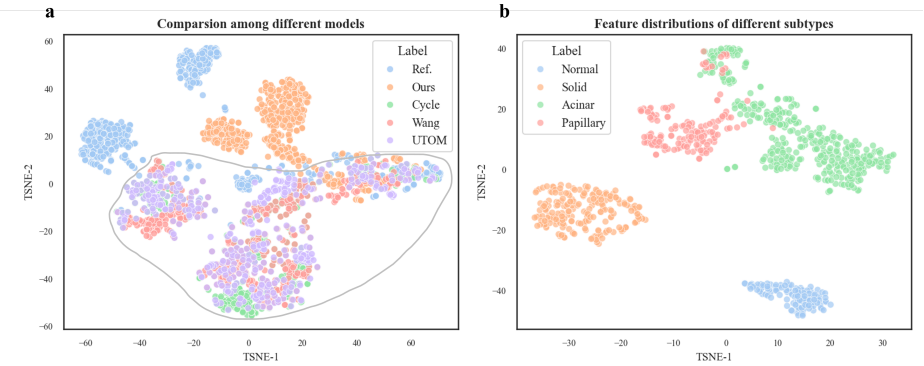

Fig. 3. Distributions of feature embedding via TSNE (t-Distributed Stochastic Neighbor Embedding).

3.4 Feature-based Quantitative Assessment of Virtual H&E

In addition to the aforementioned technical performance metrics (FID, KID, and IS), we performed an analysis of feature distribution patterns between model-generated images and references. Specifically, we conducted a comparative analysis of image embeddings extracted by PLIP from virtually stained images and their corresponding chemically stained counterparts. As illustrated in Fig. 3, the feature distributions of CycleGAN [27], Wang's model [22], and UTOM [9] exhibit substantial overlap and clustering (highlighted by the gray circle), indicating similar characteristics in their output patterns. Moreover, those three models demonstrate significant dispersion and deviation from the clinical standard staining pattern. In contrast, our method exhibits substantially closer alignment with the reference distribution, with markedly reduced discrepancies compared to other baseline models. This quantitative analysis demonstrates that our model generates H&E staining results that are more clinically relevant and visually consistent with standard references than existing approaches.

Furthermore, we assessed the distribution patterns of different LUAD subtypes using our proposed model. As illustrated in Fig. 3, distinct boundaries are observed among the subtypes. Notably, both normal and solid samples are positioned significantly distant from other subtypes, while the distributions of acinar and papillary subtypes exhibit closer proximity. This spatial arrangement

	FID↓	KID (×100)↓	IS↑
Baseline U-Net	70.74	3.77±0.16	3.49±0.07
+ PathD	61.57	<u>2.86±0.17</u>	3.75±0.07
+ SemCG	59.67	3.18±0.17	<u>3.62±0.09</u>
+ PathD + SemCG	**54.57**	**2.47±0.13**	**3.39±0.06**

*__Bold__ and <u>underlined</u> indicate the best and the second-best result, respectively.

Table 2. Ablation study on the proposed SemCG and PathD modules.

aligns with their histological characteristics: the acinar and papillary subtypes share greater morphological similarity due to their retention of glandular differentiation features and relatively organized cellular architecture. In contrast, the solid subtype, characterized by a complete loss of glandular structures and disorganized cellular arrangement, demonstrates a distinct distribution pattern. The solid subtype typically indicates a higher degree of malignancy and a poorer prognosis. The findings in Fig. 3**b** further validate the capability of our virtual staining model to provide meaningful diagnostic insights.

3.5 Ablation Study

In this study, we demonstrate that the performance of virtual staining on complex datasets, particularly unprocessed thick tissue samples, is constrained by the model's limited incorporation of essential pathological knowledge. To investigate the significance of our proposed SemCG and PathD in addressing this challenge, we conducted the ablation study on these modules. As summarized in Table 2, the integration of PathD into the baseline U-Net architecture yields a substantial improvement, with the FID score decreasing from 70.74 to 61.57. Here, the baseline model is a vanilla CycleGAN that uses a U-Net generator augmented with an attention bottleneck. Furthermore, the addition of SemCG leads to additional performance enhancements, underscoring the complementary roles of these components in improving virtual staining quality for complex thick tissue samples.

4 Conclusions

In this work, we presented a novel framework for virtual H&E staining of section-free thick tissue samples that overcomes the limitations of conventional histological staining by leveraging advanced computational imaging techniques. Our approach centers on a SemCG mechanism that robustly aligns high-level pathological features across modalities, and a PathD that enforces subtype consistency and enhances image realism through multi-scale adversarial learning and stabilization strategies. Quantitative evaluations using different metrics demonstrate that our method significantly outperforms state-of-the-art approaches, while qualitative assessments confirm that our framework preserves subtle histological details and maintains balanced stain tones. These improvements are

critical for reliable pathological interpretation and have the potential to accelerate rapid diagnostic workflows in clinical settings.

Acknowledgments. This work was supported in part by the Hong Kong Innovation and Technology Commission (ITS/023/22FP).

Disclosure of Interests. The authors have no competing interests to declare that are relevant to the content of this article.

References

1. Cao, R., Nelson, S.D., Davis, S., Liang, Y., Luo, Y., Zhang, Y., Crawford, B., Wang, L.V.: Label-free intraoperative histology of bone tissue via deep-learning-assisted ultraviolet photoacoustic microscopy. Nature biomedical engineering **7**(2), 124–134 (2023)
2. Chen, Z., Yu, W., Wong, I.H., Wong, T.T.: Deep-learning-assisted microscopy with ultraviolet surface excitation for rapid slide-free histological imaging. Biomedical Optics Express **12**(9), 5920–5938 (2021)
3. Dai, W., Wong, I.H., Wong, T.T.: Exceeding the limit for microscopic image translation with a deep learning-based unified framework. PNAS nexus **3**(4), pgae133 (2024)
4. Eberle, F.C., Mani, H., Jaffe, E.S.: Histopathology of hodgkin's lymphoma. The Cancer Journal **15**(2), 129–137 (2009)
5. Fereidouni, F., Harmany, Z.T., Tian, M., Todd, A., Kintner, J.A., McPherson, J.D., Borowsky, A.D., Bishop, J., Lechpammer, M., Demos, S.G., et al.: Microscopy with ultraviolet surface excitation for rapid slide-free histology. Nature biomedical engineering **1**(12), 957–966 (2017)
6. Glaser, A.K., Reder, N.P., Chen, Y., McCarty, E.F., Yin, C., Wei, L., Wang, Y., True, L.D., Liu, J.T.: Light-sheet microscopy for slide-free non-destructive pathology of large clinical specimens. Nature biomedical engineering **1**(7), 0084 (2017)
7. Huang, Z., Bianchi, F., Yuksekgonul, M., Montine, T.J., Zou, J.: A visual–language foundation model for pathology image analysis using medical twitter. Nature medicine **29**(9), 2307–2316 (2023)
8. Li, J., Garfinkel, J., Zhang, X., Wu, D., Zhang, Y., De Haan, K., Wang, H., Liu, T., Bai, B., Rivenson, Y., et al.: Biopsy-free in vivo virtual histology of skin using deep learning. Light: Science & Applications **10**(1), 233 (2021)
9. Li, X., Zhang, G., Qiao, H., Bao, F., Deng, Y., Wu, J., He, Y., Yun, J., Lin, X., Xie, H., et al.: Unsupervised content-preserving transformation for optical microscopy. Light: Science & Applications **10**(1), 1–11 (2021)
10. Li, Y., Pillar, N., Li, J., Liu, T., Wu, D., Sun, S., Ma, G., de Haan, K., Huang, L., Zhang, Y., et al.: Virtual histological staining of unlabeled autopsy tissue. Nature Communications **15**(1), 1684 (2024)
11. Lu, M.Y., Chen, B., Williamson, D.F., Chen, R.J., Liang, I., Ding, T., Jaume, G., Odintsov, I., Le, L.P., Gerber, G., et al.: A visual-language foundation model for computational pathology. Nature Medicine **30**, 863–874 (2024)
12. Maloney, B.W., McClatchy III, D.M., Pogue, B.W., Paulsen, K.D., Wells, W.A., Barth, R.J.: Review of methods for intraoperative margin detection for breast conserving surgery. Journal of biomedical optics **23**(10), 100901 (2018)

13. Martell, M.T., Haven, N.J., Cikaluk, B.D., Restall, B.S., McAlister, E.A., Mittal, R., Adam, B.A., Giannakopoulos, N., Peiris, L., Silverman, S., et al.: Deep learning-enabled realistic virtual histology with ultraviolet photoacoustic remote sensing microscopy. Nature Communications **14**(1), 5967 (2023)
14. Mescheder, L., Geiger, A., Nowozin, S.: Which training methods for gans do actually converge? In: International conference on machine learning. pp. 3481–3490. PMLR (2018)
15. Miyato, T., Kataoka, T., Koyama, M., Yoshida, Y.: Spectral normalization for generative adversarial networks. arXiv preprint arXiv:1802.05957 (2018)
16. Musumeci, G.: Past, present and future: overview on histology and histopathology. J Histol Histopathol **1**(5), 1–3 (2014)
17. Oord, A.v.d., Li, Y., Vinyals, O.: Representation learning with contrastive predictive coding. arXiv preprint arXiv:1807.03748 (2018)
18. Rivenson, Y., Liu, T., Wei, Z., Zhang, Y., de Haan, K., Ozcan, A.: Phasestain: the digital staining of label-free quantitative phase microscopy images using deep learning. Light: Science & Applications **8**(1), 1–11 (2019)
19. Rivenson, Y., Wang, H., Wei, Z., de Haan, K., Zhang, Y., Wu, Y., Günaydın, H., Zuckerman, J.E., Chong, T., Sisk, A.E., et al.: Virtual histological staining of unlabelled tissue-autofluorescence images via deep learning. Nature biomedical engineering **3**(6), 466–477 (2019)
20. Somerset, H.L., Kleinschmidt-DeMasters, B.K.: Approach to the intraoperative consultation for neurosurgical specimens. Advances in anatomic pathology **18**(6), 446–449 (2011)
21. Thanh-Tung, H., Tran, T., Venkatesh, S.: Improving generalization and stability of generative adversarial networks. arXiv preprint arXiv:1902.03984 (2019)
22. Wang, R., Song, P., Jiang, S., Yan, C., Zhu, J., Guo, C., Bian, Z., Wang, T., Zheng, G.: Virtual brightfield and fluorescence staining for fourier ptychography via unsupervised deep learning. Opt. Lett. **45**(19), 5405–5408 (Oct 2020). https://doi.org/10.1364/OL.400244, https://opg.optica.org/ol/abstract.cfm?URI=ol-45-19-5405
23. Wang, T.C., Liu, M.Y., Zhu, J.Y., Tao, A., Kautz, J., Catanzaro, B.: High-resolution image synthesis and semantic manipulation with conditional gans. In: Proceedings of the IEEE conference on computer vision and pattern recognition. pp. 8798–8807 (2018)
24. Ye, S., Zou, J., Huang, C., Xiang, F., Wen, Z., Wang, N., Yu, J., He, Y., Liu, P., Mei, X., et al.: Rapid and label-free histological imaging of unprocessed surgical tissues via dark-field reflectance ultraviolet microscopy. Iscience **26**(1) (2023)
25. Zhang, Y., Kang, L., Wong, I.H., Dai, W., Li, X., Chan, R.C., Hsin, M.K., Wong, T.T.: High-throughput, label-free and slide-free histological imaging by computational microscopy and unsupervised learning. Advanced Science **9**(2), 2102358 (2022)
26. Zhang, Y., Huang, L., Liu, T., Cheng, K., de Haan, K., Li, Y., Bai, B., Ozcan, A.: Virtual staining of defocused autofluorescence images of unlabeled tissue using deep neural networks. Intelligent Computing (2022)
27. Zhu, J.Y., Park, T., Isola, P., Efros, A.A.: Unpaired image-to-image translation using cycle-consistent adversarial networks. In: Proceedings of the IEEE international conference on computer vision. pp. 2223–2232 (2017)